GEOPHYSICS

Seismicity diagnostic of permeability creation from centimeter to subkilometer scales in crystalline rock during shear stimulation

Pengliang Yu[1,2]*, Agathe Eijsink[1,2,3], Junpeng Wang[2], Chris Marone[1,4], Derek Elsworth[1,2]*

Permeability evolves dynamically in the crust and mediates important natural and industrial processes in the subsurface. Episodic microearthquakes generate porosity and, thus, permeability by creating or reactivating fractures. We constrain the form of the scaling relationship linking seismic moment (M_0) to incremental permeability generation (Δk) through a series of laboratory fault reactivation experiments with absolute constraint on seismic moment. We demonstrate $\Delta k - M_0$ proportionality at centimeter scale but confirm predictive power-law scaling using a first-order model as $\Delta k = \lambda M_0^{2/3}$ from centimeter to subkilometer scale. Stress drop, fault roughness, and deformation modulus condition the prefactor λ, extending over 10 decades for reasonable natural parameter ranges. However, observed permeabilities are much more tightly constrained, with λ spanning only two orders of magnitude over length scales from centimeter to subkilometer, suggesting interdependencies in the controlling variables and rendering the relation as diagnostic in predicting fluid flow in crustal reservoirs.

INTRODUCTION

The permeability of the shallow crust decreases with depth (*1*–*3*) due to the effects of increasing confining pressure on stress-sensitive natural fractures (*4*–*6*) and the rapid healing and sealing of tectonic strain–induced damage (*7*–*10*). Crustal temperatures increase with depth, but the ability to recover geothermal heat by forced convection is intrinsically limited by low and depth-decreasing permeabilities (*2*). Elevating permeabilities through the forced shear reactivation of faults and fractures replicates the effects of enhancing the permeability in the shallow crust driven by tectonic earthquakes (*11*–*14*). This process, often referred to as shear stimulation in enhanced geothermal systems (EGS) (*15*–*17*), is fundamental in the recovery of deep geothermal resources as a sustainable energy source.

Microearthquakes (MEQs) triggered by such forced fluid injection and resulting shear stimulation (*2*) provide reliable constraints on the progress of permeability evolution and effectiveness of stimulation (*18*, *19*). Fracture permeability is typically enhanced during shear slip accompanied by shear-induced dilation and the self-propping of fractures, developing connected pathways (*20*). This suggests that changes in permeability can be diagnosed if the energy release or other features of MEQs are mechanistically linked to the creation of porosity and permeability. Establishing this linkage necessitates a mechanistic understanding of the connections between MEQs and fracture displacement, changes in fracture morphology, and related energy budgets (*20*, *21*).

Numerous studies and observations have elucidated the connections between in situ MEQ data and permeability enhancement. For example, the spatiotemporal growth of MEQ triggering fronts (*22*, *23*) and the integration of MEQ occurrence times with tracer data (*24*) can be used to estimate hydraulic diffusivity and, thereby, the effective permeability of reservoirs. Other collective statistics of MEQs, such as seismicity density and hypocenter density, have been linked with pore pressure increases to infer spatiotemporal permeability enhancement (*25*–*29*). The energy released by MEQs, codified by magnitude or seismic moment, may also be considered diagnostic of the creation of connected permeable flow pathways and, thus, permeability evolution. For instance, at the Soultz hot dry rock site in France, permeability enhancement peaked when the microseismic energy release rate was highest (*30*). Cumulative seismic moment also correlated with stimulated reservoir volume in the Habanero EGS reservoir (*31*). A detailed workflow linking MEQs to fracture aperture and permeability across various scales has been proposed to demonstrate their mechanistic connection (*12*, *32*–*34*). Recently, deep learning and transfer learning methods have successfully confirmed the linkage between features of MEQ sequences, such as seismicity rate and seismic moment, and permeability using high-quality datasets from various stimulation projects (*34*). Despite these advances, a physically inspired deterministic relationship that quantitatively and deterministically links the characteristics of MEQs with sparse permeability evolution observations is lacking. This gap highlights the need for methods to remotely measure and determine in situ permeability changes.

In this study, we explore the physics of the seismicity-permeability scaling relationships through a series of well-controlled laboratory experiments on faults in crystalline rocks. In particular, we examine whether permeability change (Δk) is indeed linearly related ($\alpha = 1$) to seismic moment (M_0) across broad length scales as $\Delta k \propto M_0^{\alpha}$. We measure the induced permeability against calibrated seismic moments from concurrent induced acoustic emission (AE) events during pressure step reactivation of laboratory faults. We use these to probe and mechanistically constrain the form of this $\Delta k \propto M_0^{\alpha}$ scaling in the laboratory and thereby extend observations over five decades of spatial length scales (centimeter to subkilometer).

RESULTS

Fault reactivation experiments

We supplement prior field scale experiments with tightly constrained reactivation experiments on laboratory faults (fig. S1) to nucleate fluid injection–induced earthquakes that increment permeabilities.

[1]EMS Energy Institute, G3 Center and Department of Geoscience, Pennsylvania State University, University Park, USA. [2]EMS Energy Institute, G3 Center and Department of Energy and Mineral Engineering, Pennsylvania State University, University Park, USA. [3]TNO Geological Survey of the Netherlands, Utrecht, Netherlands. [4]Dipartimento di Scienze della Terra, La Sapienza Università di Roma, Roma, Italy.
*Corresponding author. Email: pmy5077@psu.edu (P.Y.); elsworth@psu.edu (D.E.)

Laboratory MEQs are measured by absolutely calibrated Piezoelectric transducers (PZTs) to link observations of incremented permeabilities to seismic moment with first-order models confirming mechanistic linkages.

Representative experiment PL02 (Fig. 1) was conducted with a zero load-point displacement (ZD) boundary condition. Downstream pressure was maintained at 0.5 MPa, with the upstream pressure incrementally increased by 0.5 MPa every 3 min (Fig. 1A), allowing for a new steady flow condition.

Steady-state permeability is calculated from steady flow rate (Eq. 7; see Materials and Methods) at the end of each pressure increment (Fig. 1B) and correlated with initial shear displacement and related shear-induced AE events. As shown in Fig. 1 and in the four additional shear reactivation experiments presented in figs. S2 to S5, the largest permeability enhancements consistently correlate with the highest cumulative amplitudes of AE events. Thus, we focus on the scaling between cumulative seismic moment and permeability enhancement, with the potential to build rational and robust physics-based linkages between the two variables.

Permeability will change with incremented pressure and decremented effective stress both pre– and post–shear reactivation. We show that preslip changes in permeability are negligible and that shear slip is indeed the primary factor affecting permeability, offering the potential to functionally link permeability change to shear displacement or some other proxy, such as seismic moment. We first

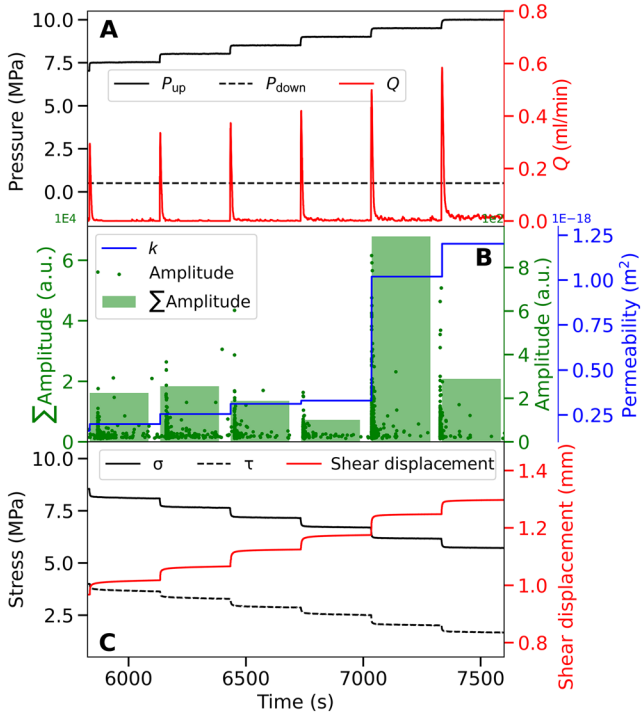

Fig. 1. Observed permeability enhancement and cumulative amplitudes of AE events during each pressure step induced by fluid injection in experiment PL02 under ZD conditions. (**A**) Prescribed histories of downstream and upstream pressure, and evolving upstream injection rate Q. (**B**) Induced AE event amplitudes, cumulative amplitude per step, and measured steady-state permeability per step. (**C**) Effective normal stress, shear stress, and shear displacement changes during the shear reactivation experiment. a.u., arbitrary unit.

measured permeability changes with normal stress without shear slip, and then, we measured both effects together. This is shown in fig. S6, where the full duration of experiment PL16_run 3 is illustrated. We analyzed the permeability evolution when slip is zero (yellow-shaded zone in fig. S6), during the first five pressure steps in which the driving effect on permeability is solely due to changes in effective normal stress. We find that the permeability changes caused by changes in effective normal stress are of the order of 1×10^{-22} m^2 (table S2). In contrast, during the subsequent pressure steps with slip (green-shaded zone), the minimum permeability change for each step is 7.34×10^{-21} m^2, which is ~10 times larger than the permeability change without slip. This clearly demonstrates that the shear slip, rather than the effective normal stress in our experiments, is the dominant contributor to permeability evolution, and, thus, the experiments and related model designed in this study that incorporate permeability enhancement driven by the mechanics of shear slip alone is appropriate.

In our experiments, we focus on the later pressure-step phase (green-shaded zone in fig. S6), during which permeability continuously increases throughout shear reactivation. We acknowledge, however, that permeability can decrease under different conditions, such as those described by Rutter and Mecklenburgh (*35*), Zhu and Wong (*36*), and Holcomb and Olsson (*37*), and through the generation of a gouge zone and wear products (*8*, *38*–*44*). For example, Im *et al.* (*8*) document that permeability in Westerly granite declines during the first few millimeters of slip due to damage of the mated contact surface and the associated production of wear materials. Our data similarly show an initial permeability reduction (yellow- and white-shaded zones in fig. S6 and table S2) that likely stems from wear-product generation during the early stress loading slip phase and shear slip in the white-shaded zone (fig. S6 and table S2). By contrast, shear dilation in the later pressure steps (green-shaded zone in fig. S6 and table S2) appears to release these wear products and mitigate clogging, ultimately resulting in a net increase in permeability. This progression is consistent with the later-stage behavior reported by Im *et al.* (*8*).

In addition, we acknowledge that substantial AE activity may be associated with compaction in highly porous sandstones (*36*, *37*), often leading to decreased permeability. However, our experiments specifically examine slip on preexisting fault surfaces in low-porosity, crystalline rocks [Westerly granite and Frontier Observatory for Research in Geothermal Energy (FORGE) granitoid], rather than porous sandstones. The porosity of the FORGE granitoid is ~1.2% (*45*), whereas the Westerly granite has a porosity of about 0.8% (*46*). For both rocks, permeability is dominated by fracture networks, with negligible contribution of the matrix. Images of the two rock types are provided in fig. S14. For detailed mechanical and hydraulic properties, we refer to Smith *et al.* (*47*) for the Utah FORGE granitoid and Lokajíček *et al.* (*48*) for Westerly granite. Under these conditions, shear displacement emerges as the primary deformation mechanism once slip initiates, and the recorded AE signals closely coincide with slip events. This slip then induces fracture dilation, thereby enhancing permeability by creating or enlarging fluid pathways (*8*, *49*, *50*).

We seek to improve on prior work that merely scales changes in permeability with seismic moment (*34*) with a linkage that is, instead, diagnostic. Thus, we establish first-order correlations to represent these carefully constrained laboratory observations linking changes in permeability with seismic moment. We then rationalize

this correlation with first-order models to recover robust and reliable predictions and then test these predictions across extended length scales, from centimeters to decameters through subkilometers.

Observed scaling between seismic moment and permeability

We calculate incremental changes in permeability as $\Delta k_i = k_i - k_{i-1}$, where k_i is the steady-state permeability at the current pressure upstep relative to k_{i-1} from the preceding pressure. Binned seismic moments (M_0) are evaluated in each pressure step (Fig. 1B) and may be correlated against permeability change (Δk) (Fig. 2) for all shear reactivations triggered in this study.

Seismic moments and permeability changes each span an order of magnitude in individual experiments (Fig. 2, B to E) and are broadly linearly proportional (Fig. 2, B to E). In the ensemble suite of five experiments, comprising 36 reactivations, this linear proportionality is maintained (Fig. 2A). Overall, this ensemble linear proportionality spans approximately three to four orders of magnitude in seismic moment and permeability and is consistent with previous characterizations inferred from field data (*34*). Thus, linear scaling is indeed suggested with $M_0 \propto \Delta k$ across the specific centimeter length scale of this laboratory fault. However, how this transits to extended scales remains unclear, and the exact form and nature of this connection is undefined.

In principle, permeability changes in shear reactivation stem from shear-induced dilation ($\Delta b \propto \Delta u$), so one might expect a direct correlation between Δk and slip. To test this hypothesis, we compared Δk and shear slip across all experiments (fig. S12). Under ZD conditions (PL02, PL03, PL16_run1, and PL16_run3), Δk broadly increases in proportion to slip, with a few outliers from PL16_run1. These outliers suggest that permeability enhancement in this experiment is not solely governed by bulk slip. One plausible explanation is that permeability is locally controlled by constrictions within the flow architecture within the fracture. In such cases, even limited shear displacement can substantially modify flow pathways if it mobilizes or removes these permeability-controlling throats.

In addition, under constant shear stress (CSS) (e.g., PL14), Δk also scales with slip but exhibits a distinctly different slope. This discrepancy indicates that permeability changes depend not only on the total slip but also on the mechanical boundary conditions. As a result, while slip may serve as a reasonable proxy for permeability changes within a single experiment or under near-identical boundary conditions, it does not generalize as robustly across varying stress states.

An additional practical consideration is that of measurability in the field. Direct measurements of slip are rarely available in near-real-time, making it challenging to link in situ slip to permeability changes during active reservoir stimulation. By comparison, cumulative seismic moment can be determined from microseismic monitoring and is thus more readily tracked. Consequently, a moment-based framework offers a unified way to estimate permeability changes across a broader spectrum of boundary conditions and scales, even though a slip-based correlation may be theoretically sound in well-constrained laboratory settings.

Diagnostic scaling between seismic moment and permeability

We attempt to define a direct quantitative link between change in permeability and seismic moment. In cases where initial permeability (k_0) is very low relative to changes driven by seismicity ($k_0 \ll \Delta k$), the permeability change may be approximated as $\Delta k \sim b^3/12s$ (*34*).

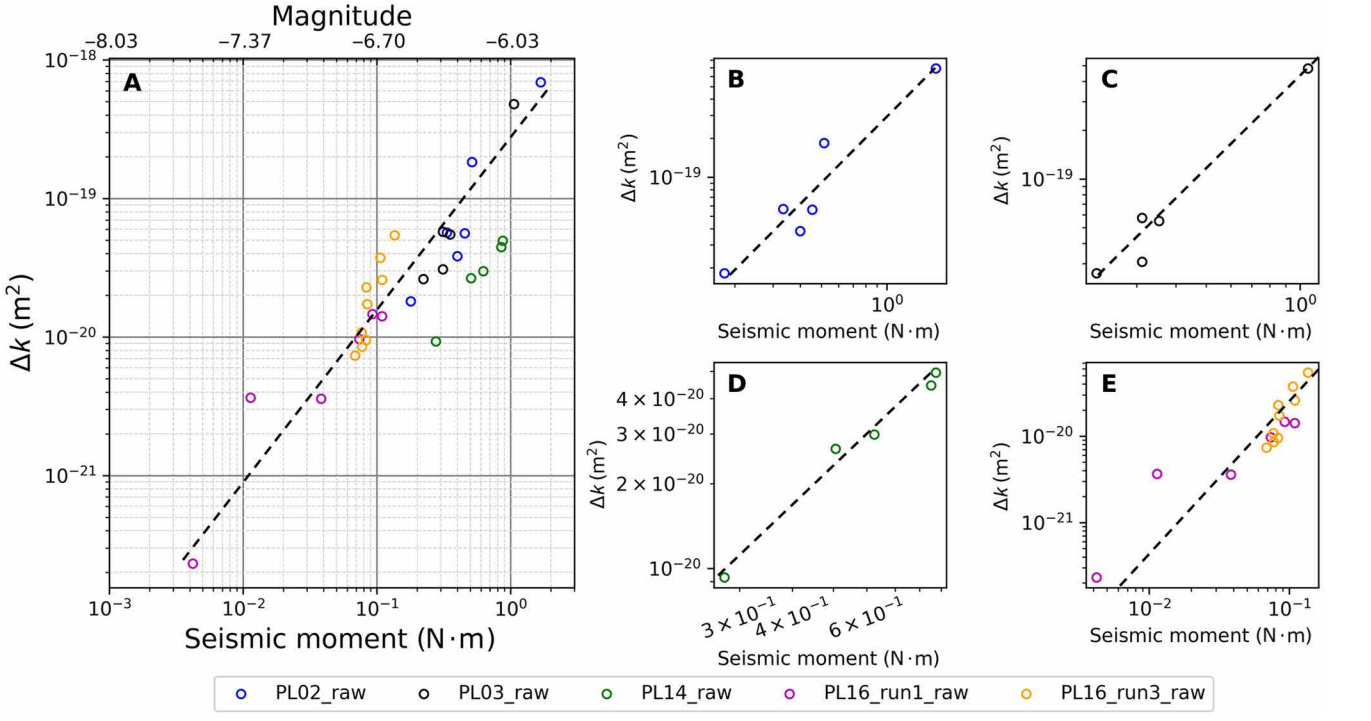

Fig. 2. Cumulative seismic moment versus calculated permeability changes for five shear reactivation experiments. (**A**) Combined data for all five experiments, showing cumulative seismic moment versus permeability changes in each pressure step. (**B** to **E**) Individual plots for each experiment, depicting the relationship between cumulative seismic moment and permeability changes for each pressure step. Dashed lines represent best fits through laboratory data.

Fracture dilation Δb may be linked to shear offset (Δu_s) across a reactivating fault as $\Delta b = \alpha \Delta u_s$, where fault roughness $\alpha = h/L$ is scale independent in our experiments and defined in terms of maximum amplitude (h) over a base/wavelength (L). Last, seismic moment (M_0) may be linked to shear modulus (G) and remobilized fault area (A) as $M_0 = GA\Delta u_s$ or to stress drop ($\Delta\tau$) and tributary volume (V) that is destressed by slip as $M_0 = V\Delta\tau$. V is used to describe the fault-destressed (or slip-activated) volume in which fluid flow is likely to be reconfigured by the slip event. At the laboratory scale, this volume is constrained by the preexisting fault geometry and the local stress field. At field scale, V relates to the extent of the slipping patch or zone that undergoes reactivation, which is tied to the cumulative moment release.

Thus, defining both permeability change Δk and seismic moment M_0 in terms of shear offset Δu_s, then equating them and then eliminating patch area A by noting that $A = V^{2/3} = \left(\frac{M}{\Delta\tau}\right)^{2/3}$ (*34*) straightforwardly yields

$$\Delta k = M_0 \Delta\tau^2 \alpha^3 / 12 s G^3 \quad (1)$$

This links permeability change Δk linearly to seismic moment (M_0) through stress drop, fault roughness, fracture spacing, and shear modulus. Shear modulus is tightly constrained in the range ~10 to 30 GPa with stress drop $\Delta\tau$ typically of the order of ~1 to ~10 MPa in nature (*51*–*53*) and ~0.3 MPa in the laboratory experiments. Fracture spacing can be observed, with the roughness amplitude-to-wavelength ratio α (*54*, *55*) for real faults typically in the range 10^{-3} to 10^{-1} (*50*, *56*–*60*). Where these parameters are known, Eq. 1 is diagnostic.

Thus, $\Delta k = \omega M_0$, with $\omega = \Delta\tau^2\alpha^3/12sG^3$, both validating and physically constraining the limited linear proportionality observed in Fig. 2. However, this linearity requires that spacing between major adjacent fractures s remains constant as well as stress drop $\Delta\tau$. A constant fracture spacing is ostensibly true for the laboratory experiments where the equivalent fracture spacing is constrained by the geometry of the sample (fig. S11). However, no such constraint can be anticipated for stress drops, which typically range over an order of magnitude or so. We note that in our experiments, stress drop is directly measured and thus constrained.

We use this measured stress drop and invariant geometry for all the laboratory experiments to independently evaluate the change in permeability from Eq. 1. The shear stress drop for each pressure step ($\Delta\tau_i$) is evaluated as $\tau_i - \tau_{i-1}$. The effective fracture spacing (s) is 3.14×10^{-2}m based on the sample geometry (fig. S11). The equivalent shear modulus (G) for the loading system is determined as $G = k_s a$, where k_s is the tangential loading stiffness measured in each experiment. a is the length of the fault in the direction of shear reactivation. Detailed derivations and measurements of k_s are provided in text S4, table S1, and fig. S10. To ensure consistent roughness, we polished the fault with #60 grit abrasive compound between experiments. This provided a constant relative roughness for all experiments as measured by focus variation optical profilometer. These measurements define a mean fault surface amplitude (h) of ~6 μm over a trace/wavelength (L) of ~600 μm corresponding to a relative roughness of $\alpha \sim 0.01$.

We compare the permeability changes (Δk_d) calculated from Eq. 1 with the experimentally measured permeability changes (Δk_{raw}) in Fig. 3 using the parameters above, showing excellent correspondence. In addition, we make a point-by-point comparison between

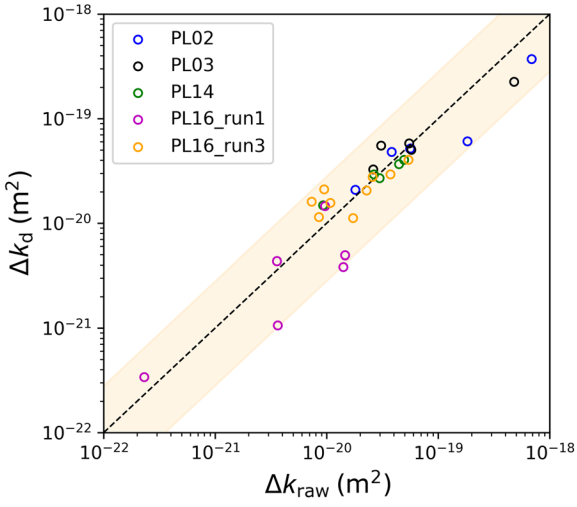

Fig. 3. Comparison between permeability changes observed in experiments and those calculated based on Eq. 1 for all shear reactivation experiments. Δk_{raw} represent the permeability changes evaluated from the steady-state period of each pressure step, with Δk_d the permeability changes calculated from laboratory measured seismic moment and stress drop based on the linear relationship defined in Eq. 1.

calculated permeability changes from Eq. 1 and those measured in experiments, plotted against seismic moments for each experiment in Fig. 4 (A to D). These results indicate an excellent fit of the model, with high R^2 values, validating the linearly proportional relationship of $\Delta k = \omega M_0$ at centimeter-scale within the laboratory experiments. Last, we show field data from the EGS Collab and Utah FORGE projects that also generally fit this linear scaling (Fig. 4E), with fitting at extended length scales discussed later.

DISCUSSION

Upscaling $\Delta k - M_0$ relationships

With the veracity and fidelity of Eq. 1 confirmed for laboratory data (Figs. 3 and 4, A to D), we explore its applicability in its extension to field scale using high-quality datasets where time histories of changes in permeability and seismicity are concurrently available. Two such datasets are from three episodes of the EGS Collab stimulation (EP3, EP4, and EP5) and the three stages of hydraulic stimulations (S1, S2, and S3) for the Utah FORGE 16A(78)-32 well. These datasets provide measurements of permeability changes and concurrent MEQs (*61*–*63*) at decameter (EGS Collab) and subkilometer (Utah FORGE) scales.

We recover permeabilities from the evolving histories of ratios of fluid injection rates to fluid overpressures (i.e., injectivities) corrected for an approximate flow length and geometry (*34*). We assume steady flow within each episode in EGS Collab and within each stage in Utah FORGE, returning a final data point representing permeability change at the end of the stimulation. The cumulative seismic moment is summed from all recorded MEQs in each episode or stage. This approach provides three $\Delta k - M_0$ observations for each of EGS Collab and Utah FORGE, as shown in Fig. 4E. As apparent, the 1:1 extension of the best fit line through the laboratory data reasonably fits the field data over their range in length scales. The fit is particularly good for the decameter EGS Collab data but

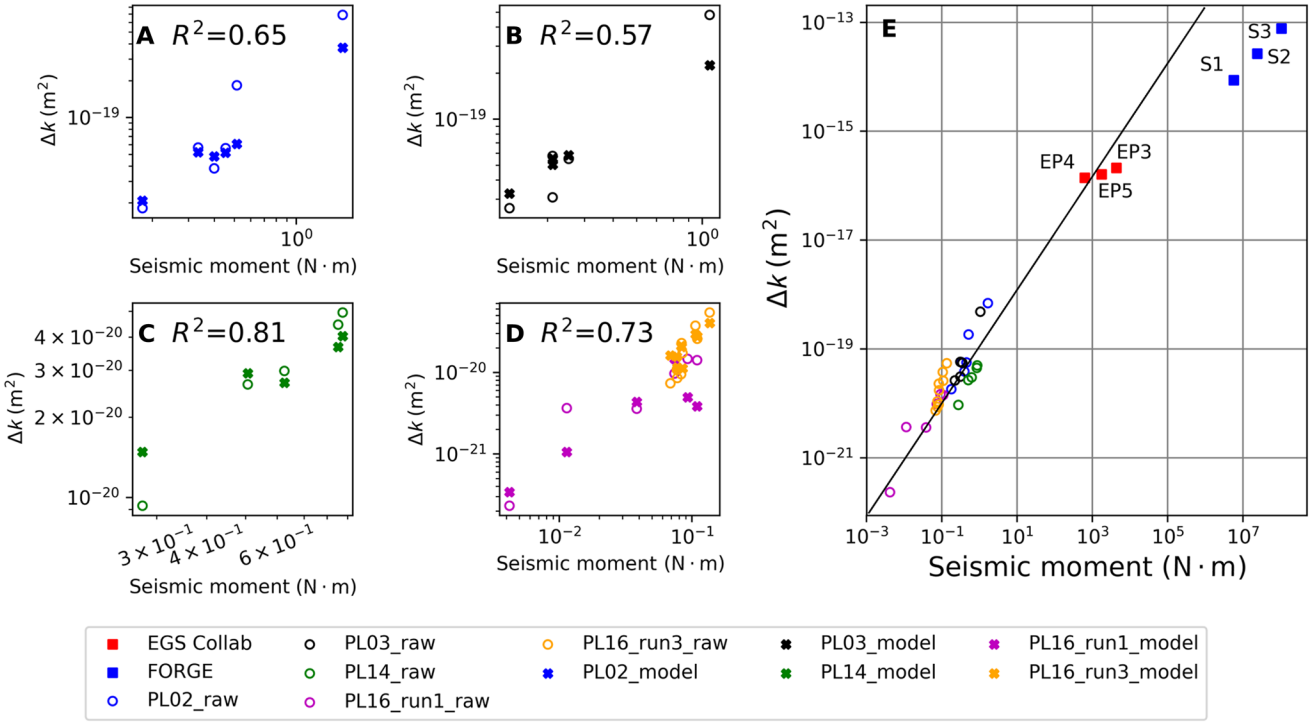

Fig. 4. Comparison of measured and calculated permeability changes based on Eq. 1 for all shear reactivation experiments. (**A** to **D**) Comparison of permeability changes from experiments and those predicted by Eq. 1, plotted against seismic moments for all shear reactivation experiments. Open circles represent raw measurements from experiments, and cross markers are changes in permeability calculated using Eq. 1. (**E**) Ensemble plot of laboratory $\Delta k - M_0$ observations with similar data collected over three stimulation episodes for the EGS Collab experiment (red squares: EP3, EP4, and EP5) and over three stages (blue squares: S1, S2, and S3) of stimulation conducted at Utah FORGE in 2022. Line represents extended best fit through laboratory data at 1:1.

less convincing for the Utah FORGE data at larger scale (see also fig. S13 and text S5).

This mismatch at larger length scales prompts a reconsideration of scaling relation. As previously noted, the deterministic prefactor ω scaling moment to permeability change ($\Delta k = \omega M_0$) is a function of shear modulus, roughness, stress drop, and fracture spacing. Of these, the shear modulus is sensibly decoupled from the size of the slipping fault patch. However, roughness, effective stress drop, and fracture spacing could be linked to patch size, particularly for small ruptures that are not much larger than the critical nucleation dimension for instability. Fault roughness across different scales is often described using the Hurst exponent H, where $\alpha = h/L^H$, with $H = 1$ indicating strict self-similarity. Some observations show fault surfaces to be largely self-affine with a Hurst exponent of $H \sim 0.8$ across various scales (*57*), with others arguing that $H = 1$ can adequately describe all resolvable scales (*54*, *64*). In this study, we adopt $H = 1$. If the slipping patch creates a high permeability pathway and destresses a tributary volume as $M \sim \Delta\tau V$, the destressed volume would comprise a sphere circumscribing a penny-shaped crack, jointly of radius a. In this case, the permeability change would be localized to the reactivated patch—fractures within the circumscribing sphere will contribute little to any permeability change. Thus, an effective spacing for the principal hydraulic conduit of the reactivated fault is sensibly at the scale of the patch radius, a, or diameter, $2a$. This is suggested in studies on fracture networks where mechanical interactions and stress shadows influence effective fracture spacing–length scaling (*65*, *66*). We select $s \sim a$.

Similarly, moment, stress drop, and patch radius are also interdependent (*53*) as

$$M_0 = \frac{16\Delta\tau}{7}a^3 \tag{2}$$

where a is the radius of the penny-shaped crack. Taking the spacing and nucleating patch radius as equivalent ($s \sim a$) and substituting Eq. 2 into Eq. 1 yield a revised power law scaling relationship between permeability change and seismic moment, as

$$\Delta k = \lambda M_0^{2/3} \tag{3}$$

with

$$\lambda = \left(\frac{16}{7}\right)^{1/3}\frac{\Delta\tau^{7/3}\alpha^3}{12G^3} \tag{4}$$

This correctly accommodates the interdependencies of seismic moment, stress drop, and effective fracture spacing (Eq. 2) on the size of the slipping patch and, thus, should better accommodate diagnostic scaling across broad ranges in length scales. This potentially allows field data, where permeability change is measured with seismic moment, to be accommodated as diagnostic of the system.

Application across scales

We examine whether the revised scaling relationship of Eqs. 3 and 4 is able to explain the spread of data of Fig. 4E. The diagnostic prefactor is conditioned by stress drop, fault roughness, and shear modulus,

all of which are reasonably tightly constrained. Stress drop $\Delta\tau$ is modulated by strength that typically extends over a range of 1 to 10 MPa (*51*–*53*). Fault roughness α has been shown to be fractal (*50*, *56*, *57*, *67*) and over ranges from microns to kilometers spanning the range from 10^{-3} to 10^{-1}. Last, shear modulus G for a broad range of rocks varies only narrowly in the range 10 to 30 GPa (*68*, *69*). These combined ranges of variables $\Delta\tau$, α, and G define the maximum (λ_{max}), minimum (λ_{min}), and intermediate anticipated magnitudes of λ in Eq. 4, as shown in Fig. 5. $\lambda_{max} = 1.1 \times 10^{-27}$ $Pa^{2/3}$ and with assumed stress drop spanning one decade, roughness two decades, and shear modulus a factor of three, the prefactor λ spans ~10 orders of magnitude.

Observations from laboratory shear experiments at centimeter scale, EGS Collab at decameter scale, and Utah FORGE at barely subkilometer scale all fall across the range 10^{-3} to $10^{-1}\lambda_{max}$ (Fig. 5) for $\Delta k = \lambda M_0^{2/3}$ and with no bias for length scale. This two-decade range is particularly small considering the potential 10-decade span noted for sensible ranges of stress drop, roughness, and deformability. Conversely, for the linear relationship $\Delta k = \omega M_0$, there is a progressive bias with ω systematically decreasing with increasing length scale, although this span for $\omega$is only slightly broader than that for λ at three decades. This reflects the reality that the seismic moment is not independent of stress drop and effective fracture size. These interdependencies are accommodated in the power-law model but neglected for the linear relation. Thus, the power-law scaling relationship $\Delta k \propto M_0^{2/3}$ appears the more appropriate in representing response across a broad range of different scales. This is further supported by regression against $\Delta k = \eta M_0^{\beta}$ to recover the power law exponents β for the laboratory (~1) and field (0.53) data and then for the two datasets combined (0.79) (text S5), supporting the contention that $\beta \sim \frac{2}{3}$ scaling is physically justified across scales. For sensibly near-invariant shear modulus, a decreasing prefactor λ represents decreasing stress drop and roughness. The lowest magnitudes for the prefactor are thus consistent with the manifestation of the smooth laboratory fault and quantitatively congruent with the controlled measurements.

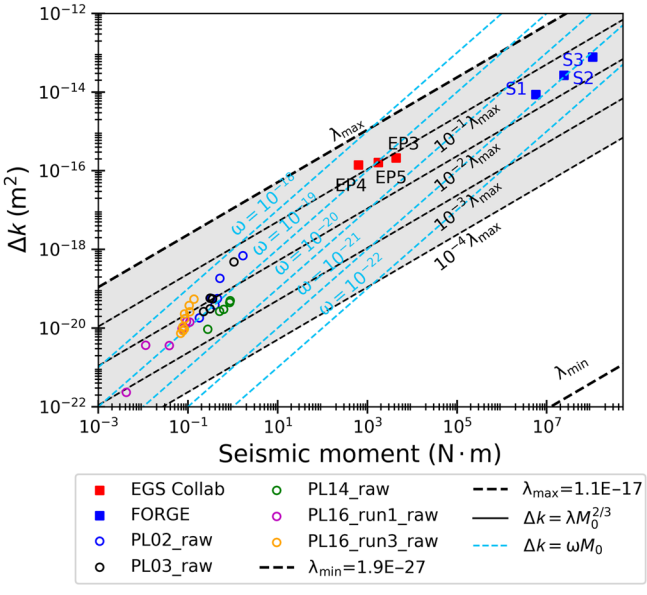

Fig. 5. Permeability changes versus seismic moment for ensemble data from laboratory to field scale. Laboratory data (open symbols) are augmented by EGS Collab (red squares) and Utah FORGE (blue squares) datasets. Blue short-dashed lines indicate the linear relationship between permeability change and seismic moment ($\Delta k = \omega M_0$) for different ω. Black long-dashed lines show the power-law scaling relationship ($\Delta k = \lambda M_0^{2/3}$) for different λ. λ_{max} and λ_{min} are determined from Eq. 4, based on $\Delta\tau$ in the range of 1 to 10 MPa, α in the range of 10^{-3} to 10^{-1}, and G in the range of 10 to 30 GPa.

While our laboratory experiments use a consistent fault surface roughness ($\alpha \sim 0.01$) using #60 grit preparation, we acknowledge that this introduces a characteristic length scale that does not replicate the scale-invariant (fractal) roughness typically observed in natural faults, although our length scale remains invariant in the experiments. As a result, the findings at the laboratory scale may not fully capture roughness-driven variability present at larger scales. However, in our cross-scale scaling analysis, we address this limitation by incorporating a range of plausible roughness values into the prefactor λ of the proposed power-law scaling, enabling us to evaluate permeability evolution across scales despite the absence of direct field-scale roughness measurements. Future studies could explore roughness variability more explicitly to further constrain scaling behavior.

For scaling against $M_0^{2/3}$, the systematic increase in λ for the EGS Collab data over the laboratory and Utah FORGE observations is small (approximately one order of magnitude) but could be attributed to the distinct characteristics of this experiment. The EGS Collab experiment is in schist, not granite, with corresponding differences in frictional properties, although the elevated λ for the schist would suggest a higher stress drop and is likely inconsistent with an anticipated lower frictional strength for the schist (*33*). Rather, a volumetric reactivation of the fracture network at EGS Collab compared to the perceived planar ensemble fracture at Utah FORGE and the known planar fault in the laboratory presents a consistent view of this discrepancy in λ. The EGS Collab test bed is characterized by notable geological heterogeneity, involving a complex metamorphic basement composed of quartz, carbonate, and schist. These rocks exhibit a wide range of mechanical properties, leading to high spatial variability in natural fractures. This heterogeneity fosters intricate interactions between hydraulic and natural fractures, often resulting in a more complex fracture network during stimulation (*61*, *70*). In contrast, the Utah FORGE site is located in a homogeneous crystalline rock formation with minimal lithological and structural discontinuities (*63*, *71*). This homogeneity tends to produce planar fracture geometries, particularly evident in the Stage 2 and Stage 3 stimulations, which were conducted within a 6-m perforated interval. In addition, Stage 3 included the injection of proppant to enhance fracture conductivity (*63*).

Similarly, the observed linear relationship between seismic moment and permeability change ($\Delta k = \omega M_0$) linking the laboratory and EGS Collab data may be attributed to the relatively small jump in scale from laboratory to decameter scale. Thus, the interdependencies of moment, stress drop, patch size, and effective fracture spacing can be neglected. However, the power-law scaling $\Delta k \propto M_0^{2/3}$ is important to incorporate as the length scale further grows.

Overall, this work builds on previous observations that observed changes in crustal permeabilities scale in a robust manner with cumulative seismic moment (*34*). This result is underpinned by the mechanistic connection between changes in fracture aperture that control permeability and are in turn controlled by shear reactivation

and indexed through energy release and associated seismic moment. This logical connection infers a linear scaling $\Delta k = \omega M_0$ confirmed over a limited range of length scales by field observations (*34*). Extending the scales of measurements and augmenting with highly constrained observations confirms the general form of this scaling but refining its true form as $\Delta k = \lambda M_0^{2/3}$ reveals the prefactor to be a diagnostic constant, suggesting the prospects for a priori predictions. Experiments and analyses confirm that this relation is supported by observations and appears relevant over length scales spanning centimeters to subkilometers. Thus, this model provides a consistent view in understanding the evolution of permeability in low-permeability crustal rocks as driven by, and in driving, seismicity.

MATERIALS AND METHODS

All laboratory experiments were conducted on a saw-cut single inclined fault transecting a cylindrical core (2.5-cm diameter and 5-cm length) inclined at 30° to the longitudinal axis. Samples were of Westerly granite and Utah FORGE granitoid with the fault surface reproducibly roughened between experiments using #60 grit abrasive powder. All experiments were at ambient temperature and follow a similar protocol. Figure S6 shows a typical cycle for a single experiment. The cores were hydraulically isolated with double latex jackets and hydrostatically loaded to 10 MPa with excess shear prestress then applied to ~80% of strength.

Two alternate boundary conditions were applied: CSS and ZD. The CSS configuration represented a condition where faults are continuously loaded by the tectonic stresses and fault displacement does not relieve shear stress. The ZD condition simulated stress relaxation during slip, where elastic strain energy is dissipated by the shear stress drop. In both modes, fault slip is triggered by stepwise incremented pore pressures. These two loading conditions bracket possible stress evolutions that a fault might experience during injection-driven reactivation (constant tectonic stress versus zero far-field deformation).

In each of these CSS and ZD modes, upstream pore pressures are incremented (0.5 MPa per 3- to 5-min step) to reactivate the fault, while holding downstream pressure constant or holding constant pressure differences between upstream and downstream (text S1). Fluid (deionized water) flows along the fault with the upstream pressure stepwise incremented to trigger fault reactivation (MEQs) and establish a new steady-state flow regime where the updated permeability is measured (fig. S4). Detailed information chronicling each experiment is in table S1. Fault shear displacement was measured together with AEs from the absolutely calibrated PZT sensors located at the sample ends (fig. S1). These PZT sensors recorded AE events associated with injection-induced fault slip. The passive AE signals recorded from downstream are used in this study.

Flow rate along the laboratory fault/fracture can be expressed as (*38*, *72*)

$$Q = \frac{wb^3}{12\mu}\frac{\Delta P}{l} \tag{5}$$

where ΔP is the differential pressure between upstream (P_{up}) and downstream (P_{down}), μ is the dynamic viscosity of water, w is the fracture width (equal to the sample diameter), l is the fracture length (distance between upstream and downstream drill holes minus the evolving cumulative shear displacement l_s), and b is the fracture aperture. The overall equivalent bulk permeability, k, may be calculated from the cubic law as (*73*)

$$k = \frac{b^3}{12s} \tag{6}$$

where s is the spacing to phantom parallel faults in the sample (fig. S11), set to first order as a large fraction of the sample diameter. The term s enables us to translate fracture aperture measurements into an equivalent bulk permeability of a ubiquitously fractured rock mass, acknowledging that the spacing of fractures in the fracture network can strongly influence fluid flow. By substituting b in Eq. 5 to Eq. 6, we recover

$$k = \frac{Q\mu l}{w\Delta P s} \tag{7}$$

While this indirect method provides a measurement of permeability and estimation of hydraulic-aperture evolution during shear stimulation, it assumes idealized flow conditions and homogeneous aperture distributions, which may not reflect localized asperity contact, gouge development, or evolving fracture surface roughness. Furthermore, this approach yields an effective aperture that reflects the hydraulic transmissivity of the entire fault, not the true mechanical separation between fracture walls (*74*). Direct aperture measurements would improve constraints on mechanics of fracture slip and opening but are not available here.

Fault slip is driven by reduced fault strength resulting from incremented mean fluid pressures and diminishing shear stress as the system unloads (ZD condition). Thus, the fault reactivates and then stabilizes once frictional resistance and the diminishing driving shear forces come into balance (Fig. 1B), allowing steady flow conditions to probe incremented permeability. AE events are detected using a long-term average/short-term average algorithm. The majority of AE events are observed to accompany the shear displacement during each pressure step, corresponding to the application of increased upstream pressure. We evaluate the seismic moments for each individual AE event from the absolute calibration and then sum them within the full period until the subsequent pressure step. For detailed calculations of effective normal stress and shear stress, together with the evaluation of seismic moment from the AE record, refer to texts S2 and S3.

Supplementary Materials

This PDF file includes:

Supplementary Text
Figs. S1 to S14
Tables S1 and S2
References

REFERENCES

1. S. E. Ingebritsen, C. E. Manning, Permeability of the continental crust: Dynamic variations inferred from seismicity and metamorphism. *Geofluids* **10**, 193–205 (2010).
2. M. Manga, I. Beresnev, E. E. Brodsky, J. E. Elkhoury, D. Elsworth, S. E. Ingebritsen, D. C. Mays, C. Y. Wang, Changes in permeability caused by transient stresses: Field observations, experiments, and mechanisms. *Rev. Geophys.* **50**, doi.org/10.1029/2011RG000382 (2012).
3. C. E. Manning, S. E. Ingebritsen, Permeability of the continental crust: Implications of geothermal data and metamorphic systems. *Rev. Geophys.* **37**, 127–150 (1999).
4. A. F. Gangi, Variation of whole and fractured porous rock permeability with confining pressure. *Int. J. Rock Mech. Min. Sci. Geomech. Abstr.* **15**, 249–257 (1978).
5. C. A. Morrow, D. A. Lockner, Permeability differences between surface-derived and deep drillhole core samples. *Geophys. Res. Lett.* **21**, 2151–2154 (1994).

6. C. Pearson, The relationship between microseismicity and high pore pressures during hydraulic stimulation experiments in low permeability granitic rocks. *J. Geophys. Res. Solid Earth* **86**, 7855–7864 (1981).
7. L. B. Hunfeld, J. Chen, S. Hol, A. R. Niemeijer, C. J. Spiers, Healing behavior of simulated fault gouges from the Groningen gas field and implications for induced fault reactivation. *J. Geophys. Res. Solid Earth* **125**, e2019JB018790 (2020).
8. K. Im, D. Elsworth, Y. Fang, The influence of preslip sealing on the permeability evolution of fractures and faults. *Geophys. Res. Lett.* **45**, 166–175 (2018).
9. M. P. Olsen, C. H. Scholz, A. Léger, Healing and sealing of a simulated fault gouge under hydrothermal conditions: Implications for fault healing. *J. Geophys. Res. Solid Earth* **103**, 7421–7430 (1998).
10. H. Yasuhara, Evolution of permeability in a natural fracture: Significant role of pressure solution. *J. Geophys. Res.* **109**, doi.org/10.1029/2003JB002663 (2004).
11. P. Yu, D. Dempsey, R. Archer, A three-dimensional coupled thermo-hydro-mechanical numerical model with partially bridging multi-stage contact fractures in horizontal-well enhanced geothermal system. *Int. J. Rock Mech. Min. Sci.* **143**, 104787 (2021).
12. Y. Fang, D. Elsworth, T. T. Cladouhos, Reservoir permeability mapping using microearthquake data. *Geothermics* **72**, 83–100 (2018).
13. Y. Guglielmi, F. Cappa, J. P. Avouac, P. Henry, D. Elsworth, Seismicity triggered by fluid injection-induced aseismic slip. *Science* **348**, 1224–1226 (2015).
14. E. L. Majer, R. Baria, M. Stark, S. Oates, J. Bommer, B. Smith, H. Asanuma, Induced seismicity associated with enhanced geothermal systems. *Geothermics* **36**, 185–222 (2007).
15. J. W. Tester, B. J. Anderson, A. S. Batchelor, D. D. Blackwell, R. DiPippo, "The Future of Geothermal Energy—Impact of Enhanced Geothermal Systems (EGS) on the United States in the 21st Century" (Rep. INL/EXT-06-11746, Mass. Inst. of Technol., 2006).
16. D. Dempsey, S. Kelkar, N. Davatzes, S. Hickman, D. Moos, Numerical modeling of injection, stress and permeability enhancement during shear stimulation at the Desert Peak Enhanced Geothermal System. *Int. J. Rock Mech. Min. Sci.* **78**, 190–206 (2015).
17. J. Samuelson, D. Elsworth, C. Marone, Shear-induced dilatancy of fluid-saturated faults: Experiment and theory. *J. Geophys. Res. Solid Earth* **114**, doi.org/10.1029/2008JB006273 (2009).
18. G. Izadi, D. Elsworth, The influence of thermal-hydraulic-mechanical- and chemical effects on the evolution of permeability, seismicity and heat production in geothermal reservoirs. *Geothermics* **53**, 385–395 (2015).
19. P. Yu, D. Dempsey, R. Archer, C. Marone, D. Elsworth, "Numerical modeling of permeability enhancement and induced seismicity during EGS operation using a partially bridging multi-stage hydraulic fracture design" in *World Geothermal Congress 2023* (2023), pp. 1–12.
20. T. Ishibashi, D. Elsworth, Y. Fang, J. Riviere, B. Madara, H. Asanuma, N. Watanabe, C. Marone, Friction-stability-permeability evolution of a fracture in granite. *Water Resour. Res.* **54**, 9901–9918 (2018).
21. T. Ishibashi, H. Asanuma, Y. Fang, C. Wang, D. Elsworth, "Exploring the link between permeability and strength evolution during fracture shearing" in *50th U.S. Rock Mechanics/Geomechanics Symposium*, Houston, Texas, June 2016 (ARMA, 2016); onepetro.org/ARMAUSRMS/proceedings/ARMA16/ARMA16/ARMA-2016-423/126288.
22. S. A. Shapiro, E. Huenges, G. Borm, Estimating the crust permeability from fluid-injection-induced seismic emission at the KTB site. *Geophys. J. Int.* **131**, 15–23 (1997).
23. S. A. Shapiro, C. Dinske, E. Rothert, Hydraulic-fracturing controlled dynamics of microseismic clouds. *Geophys. Res. Lett.* **33**, doi.org/10.1029/2006GL026365 (2006).
24. J. Chen, T. Xu, X. Liang, Z. Jiang, Stochastic inversion of tracer test data with seismicity constraint for permeability imaging in enhanced geothermal reservoirs. *Geophysics* **87**, M307–M319 (2022).
25. J. Riffault, D. Dempsey, S. Karra, R. Archer, Microseismicity cloud can be substantially larger than the associated stimulated fracture volume: The case of the Paralana Enhanced Geothermal System. *J. Geophys. Res. Solid Earth* **123**, 6845–6870 (2018).
26. J. Riffault, D. Dempsey, R. Archer, "Microearthquake enhanced permeability imaging of a stimulated well" in *53rd U.S. Rock Mechanics/Geomechanics Symposium*, New York City, New York, June 2019 (ARMA, 2019); onepetro.org/ARMAUSRMS/proceedings/ARMA19/ARMA19/ARMA-2019-0106/124623.
27. M. Tarrahi, B. Jafarpour, A. Ghassemi, Integration of microseismic monitoring data into coupled flow and geomechanical models with ensemble Kalman filter. *Water Resour. Res.* **51**, 5177–5197 (2015).
28. M. Tarrahi, B. Jafarpour, Inference of permeability distribution from injection-induced discrete microseismic events with kernel density estimation and ensemble Kalman filter. *Water Resour. Res.* **48**, doi.org/10.1029/2012WR011920 (2012).
29. P. Yu, D. Dempsey, A. P. Rinaldi, A. Calibugan, V. A. Ritz, R. Archer, Association between injection and microseismicity in geothermal fields with multiple wells: Data-driven modeling of Rotokawa, New Zealand, and Húsmúli, Iceland. *J. Geophys. Res. Solid Earth* **128**, e2022JB025952 (2023).
30. K. F. Evans, H. Moriya, H. Niitsuma, R. H. Jones, W. S. Phillips, A. Genter, J. Sausse, R. Jung, R. Baria, Microseismicity and permeability enhancement of hydrogeologic structures during massive fluid injections into granite at 3 km depth at the Soultz HDR site. *Geophys. J. Int.* **160**, 389–412 (2005).
31. E. Rothert, S. Baisch, Passive Seismic Monitoring: Mapping Enhanced Fracture Permeability. *Proc. World Geotherm. Congr.*, 25–29. (2010); https://pangea.stanford.edu/ERE/db/IGAstandard/record_detail.php?id=6706.
32. T. Ishibashi, N. Watanabe, H. Asanuma, N. Tsuchiya, Linking microearthquakes to fracture permeability change: The role of surface roughness. *Geophys. Res. Lett.* **43**, 7486–7493 (2016).
33. Z. Li, D. Elsworth, C. Wang, Induced microearthquakes predict permeability creation in the brittle crust. *Front. Earth Sci.* **10**, 1020294 (2022).
34. P. Yu, A. Mali, T. Velaga, A. Bi, J. Yu, C. Marone, P. Shokouhi, D. Elsworth, Crustal permeability generated through microearthquakes is constrained by seismic moment. *Nat. Commun.* **15**, 2057 (2024).
35. E. H. Rutter, J. Mecklenburgh, Influence of normal and shear stress on the hydraulic transmissivity of thin cracks in a tight quartz sandstone, a granite, and a shale. *J. Geophys. Res. Solid Earth* **123**, 1262–1285 (2018).
36. W. Zhu, T. Wong, The transition from brittle faulting to cataclastic flow: Permeability evolution. *J. Geophys. Res. Solid Earth* **102**, 3027–3041 (1997).
37. D. J. Holcomb, W. A. Olsson, Compaction localization and fluid flow. *J. Geophys. Res. Solid Earth* **108**, doi.org/10.1029/2001JB000813 (2003).
38. I. Faoro, A. Niemeijer, C. Marone, D. Elsworth, Influence of shear and deviatoric stress on the evolution of permeability in fractured rock. *J. Geophys. Res. Solid Earth* **114**, doi.org/10.1029/2007JB005372 (2009).
39. D. R. Faulkner, A model for the variation in permeability of clay-bearing fault gouge with depth in the brittle crust. *Geophys. Res. Lett.* **31**, doi.org/10.1029/2004GL020736 (2004).
40. M. J. Ikari, D. M. Saffer, C. Marone, Frictional and hydrologic properties of clay-rich fault gouge. *J. Geophys. Res. Solid Earth* **114**, doi.org/10.1029/2008JB006089 (2009).
41. E. H. Rutter, J. Mecklenburgh, Hydraulic conductivity of bedding-parallel cracks in shale as a function of shear and normal stress. *Geol. Soc. Spec. Publ.* **454**, 67–84 (2017).
42. E. Rutter, A. Hackston, On the effective stress law for rock-on-rock frictional sliding, and fault slip triggered by means of fluid injection. *Philos. Trans. R. Soc. A Math. Phys. Eng. Sci.* **375**, 20160001 (2017).
43. L. W. Teufel, "Permeability Changes During Shear Deformation Of Fractured Rock" in *28th U.S. Symposium on Rock Mechanics (USRMS)*, Tucson, Arizona, June 1987 (ARMA, 1987); onepetro.org/ARMAUSRMS/proceedings/ARMA87/ARMA87/ARMA-87-0473/129785.
44. S. Zhang, T. E. Tullis, The effect of fault slip on permeability and permeability anisotropy in quartz gouge. *Tectonophysics* **295**, 41–52 (1998).
45. M. Gwynn, Utah FORGE: Rock Properties, Geothermal Data Repository, Energy and Geoscience Institute at the University of Utah (2018); https://doi.org/10.15121/1452765.
46. C. Petrini, C. Madonna, T. Gerya, Inversion in the permeability evolution of deforming Westerly granite near the brittle–ductile transition. *Sci. Rep.* **11**, 24027 (2021).
47. J. T. Smith, E. L. Sonnenthal, N. Nakata, "Thermal hydrological mechanical modelling of anticipated stimulation in Utah" in *Proceedings of the 49th Workshop on Geothermal Reservoir Engineering* (Stanford Geothermal Program, 2024).
48. T. Lokajíček, D. Řimnáčová, M. Petružálek, R. Přikryl, V. Natherová, M. Racek, A. Aminzadeh, "Westerly granite study of physical and transport properties monitored by P and S waves on spherical samples: Effect of temperature and hydrostatic pressure" in *58th U.S. Rock Mechanics/Geomechanics Symposium 2024* (ARMA, 2024); doi: 10.56952/ARMA-2024-0553.
49. T. Ishibashi, H. Asanuma, Investigating geophysical indicators of permeability change during laboratory hydraulic shearing of granitic fractures with surface roughness. *Rock Mech. Rock Eng.* **57**, 5431–5445 (2024).
50. T. Ishibashi, H. Asanuma, Y. Mukuhira, N. Watanabe, Laboratory hydraulic shearing of granitic fractures with surface roughness under stress states of EGS: Permeability changes and energy balance. *Int. J. Rock Mech. Min. Sci.* **170**, 105512 (2023).
51. S. D. Goodfellow, R. P. Young, A laboratory acoustic emission experiment under in situ conditions. *Geophys. Res. Lett.* **41**, 3422–3430 (2014).
52. Y. Huang, W. L. Ellsworth, G. C. Beroza, Stress drops of induced and tectonic earthquakes in the central United States are indistinguishable. *Sci. Adv.* **3**, e1700772 (2017).
53. H. Kanamori, D. L. Anderson, Theoretical basis of some empirical relations in seismology. *Bull. Seismol. Soc. Am.* **65**, 1073–1095 (1975).
54. E. R. Heimisson, Crack to pulse transition and magnitude statistics during earthquake cycles on a self-similar rough fault. *Earth Planet. Sci. Lett.* **537**, 116202 (2020).
55. W. L. Power, T. E. Tullis, Euclidean and fractal models for the description of rock surface roughness. *J. Geophys. Res.* **96**, 415–424 (1991).
56. W. L. Power, T. E. Tullis, S. R. Brown, G. N. Boitnott, C. H. Scholz, Roughness of natural fault surfaces. *Geophys. Res. Lett.* **14**, 29–32 (1987).
57. T. Candela, F. Renard, Y. Klinger, K. Mair, J. Schmittbuhl, E. E. Brodsky, Roughness of fault surfaces over nine decades of length scales. *J. Geophys. Res. Solid Earth* **117**, doi.org/10.1029/2011JB009041 (2012).

58. S. R. Brown, Fluid flow through rock joints: The effect of surface roughness. *J. Geophys. Res. Solid Earth* **92**, 1337–1347 (1987).
59. S. R. Brown, C. H. Scholz, Closure of random elastic surfaces in contact. *J. Geophys. Res. Solid Earth* **90**, 5531–5545 (1985).
60. D. Morad, Z. Reches, A. Sagy, Y. H. Hatzor, Energy dissipation during shear along experimental rough faults. *J. Geophys. Res. Solid Earth* **129**, e2023JB028605 (2024).
61. P. Fu, M. Schoenball, J. B. Ajo-Franklin, C. Chai, M. Maceira, J. P. Morris, H. Wu, H. Knox, P. C. Schwering, M. D. White, J. A. Burghardt, C. E. Strickland, T. C. Johnson, V. R. Vermeul, P. Sprinkle, B. Roberts, C. Ulrich, Y. Guglielmi, P. J. Cook, P. F. Dobson, T. Wood, L. P. Frash, L. Huang, M. D. Ingraham, J. S. Pope, M. M. Smith, G. Neupane, T. W. Doe, W. M. Roggenthen, R. Horne, A. Singh, M. D. Zoback, H. Wang, K. Condon, A. Ghassemi, H. Chen, M. W. McClure, G. Vandine, D. Blankenship, T. J. Kneafsey, EGS Collab Team, Close observation of hydraulic fracturing at EGS Collab Experiment 1: Fracture trajectory, microseismic interpretations, and the role of natural fractures. *J. Geophys. Res. Solid Earth* **126**, e2020JB020840 (2021).
62. M. Schoenball, J. B. Ajo-Franklin, D. Blankenship, C. Chai, A. Chakravarty, P. Dobson, C. Hopp, T. Kneafsey, H. A. Knox, M. Maceira, M. C. Robertson, P. Sprinkle, C. Strickland, D. Templeton, P. C. Schwering, C. Ulrich, T. Wood, The EGS Collab Team, Creation of a mixed-mode fracture network at mesoscale through hydraulic fracturing and shear stimulation. *J. Geophys. Res. Solid Earth* **125**, e2020JB019807 (2020).
63. J. McLennan, K. England, P. Rose, J. Moore, B. Barker, "Stimulation of a high-temperature granitic reservoir at the Utah FORGE site" in *Society of Petroleum Engineers—SPE Hydraulic Fracturing Technology Conference and Exhibition 2023* (HFTC, 2023); https://dx.doi.org/10.2118/212346-MS.
64. Z. Shi, S. M. Day, Rupture dynamics and ground motion from 3-D rough-fault simulations. *J. Geophys. Res. Solid Earth* **118**, 1122–1141 (2013).
65. P. A. Gillespie, C. B. Howard, J. J. Walsh, J. Watterson, Measurement and characterisation of spatial distributions of fractures. *Tectonophysics* **226**, 113–141 (1993).
66. J. E. Olson, Sublinear scaling of fracture aperture versus length: An exception or the rule? *J. Geophys. Res. Solid Earth* **108**, doi.org/10.1029/2001JB000419 (2003).
67. S. R. Brown, C. H. Scholz, Broad bandwidth study of the topography of natural rock surfaces. *J. Geophys. Res. Solid Earth* **90**, 12575–12582 (1985).
68. W. G. Pariseau, Design Analysis in Rock Mechanics (CRC Press, ed. 3, 2017).
69. E. Hoek, J. D. Bray, Rock Slope Engineering (CRC Press, 1981).
70. K. J. Condon, H. Sone, H. F. Wang, J. Ajo-Franklin, T. Baumgartner, K. Beckers, D. Blankenship, A. Bonneville, L. Boyd, S. Brown, J. A. Burghardt, C. Chai, Y. Chen, B. Chi, K. Condon, P. J. Cook, D. Crandall, P. F. Dobson, T. Doe, C. A. Doughty, D. Elsworth, J. Feldman, Z. Feng, A. Foris, L. P. Frash, Z. Frone, P. Fu, K. Gao, A. Ghassemi, Y. Guglielmi, B. Haimson, A. Hawkins, J. Heise, C. Hopp, M. Horn, R. N. Horne, J. Horner, M. Hu, H. Huang, L. Huang, K. J. Im, M. Ingraham, E. Jafarov, R. S. Jayne, S. E. Johnson, T. C. Johnson, B. Johnston, K. Kim, D. K. King, T. Kneafsey, H. Knox, J. Knox, D. Kumar, M. Lee, K. Li, Z. Li, M. Maceira, P. Mackey, N. Makedonska, E. Mattson, M. W. McClure, J. McLennan, C. Medler, R. J. Mellors, E. Metcalfe, J. Moore, C. E. Morency, J. P. Morris, T. Myers, S. Nakagawa, G. Neupane, G. Newman, A. Nieto, C. M. Oldenburg, T. Paronish, R. Pawar, P. Petrov, B. Pietzyk, R. Podgorney, Y. Polsky, J. Pope, S. Porse, J. C. Primo, C. Reimers, B. Q. Roberts, M. Robertson, W. Roggenthen, J. Rutqvist, D. Rynders, M. Schoenball, P. Schwering, V. Sesetty, C. S. Sherman, A. Singh, M. M. Smith, H. Sone, E. L. Sonnenthal, F. A. Soom, P. Sprinkle, C. E. Strickland, J. Su, D. Templeton, J. N. Thomle, V. R. Tribaldos, C. Ulrich, N. Uzunlar, A. Vachaparampil, C. A. Valladao, W. Vandermeer, G. Vandine, D. Vardiman, V. R. Vermeul, J. L. Wagoner, H. F. Wang, J. Weers, N. Welch, J. White, M. D. White, P. Winterfeld, T. Wood, S. Workman, H. Wu, Y. S. Wu, E. C. Yildirim, Y. Zhang, Y. Q. Zhang, Q. Zhou, M. D. Zoback, Low static shear modulus along foliation and its influence on the elastic and strength anisotropy of Poorman Schist Rocks, Homestake Mine, South Dakota. *Rock Mech. Rock Eng.* **53**, 5257–5281 (2020).
71. A. Abubakar, A. Hakami, B. E. Hornby, Hydraulic fracture width determination using integration of Stoneley wave "pressure testing" with electrical borehole scans in FORGE Geothermal project, in *Proceedings, Second International Meeting for Applied Geoscience and Energy* (SEG Technical Program Expanded Abstracts, 2022); https://doi.org/10.1190/image2022-3746406.1.
72. Z. Ye, A. Ghassemi, Injection-induced shear slip and permeability enhancement in granite fractures. *J. Geophys. Res. Solid Earth* **123**, 9009–9032 (2018).
73. Z. Ouyang, D. Elsworth, Evaluation of groundwater flow into mined panels. *Int. J. Rock Mech. Min. Sci.* **30**, 71–79 (1993).
74. A. R. Piggott, D. Elsworth, Laboratory assessment of the equivalent apertures of a rock fracture. *Geophys. Res. Lett.* **20**, 1387–1390 (1993).
75. G. C. McLaskey, D. A. Lockner, B. D. Kilgore, N. M. Beeler, A robust calibration technique for acoustic emission systems based on momentum transfer from a ball drop. *Bull. Seismol. Soc. Am.* **105**, 257–271 (2015).
76. G. Foulger, R.E. Long, Anomalous focal mechanisms: Tensile crack formation on an accreting plate boundary. *Nature*, **310**, 43–45 (1984).
77. A. McGarr, Maximum magnitude earthquakes induced by fluid injection. *J. Geophys. Res. Solid Earth* **119**, 1008–1019 (2014).

Acknowledgments: We thank the editor and reviewers for the constructive review that significantly improved this manuscript. We thank S. Swavely for laboratory technical support and J. Yang for the help on conducting the ball drop experiments. **Funding:** This work is a partial result of support from the US Department of Energy under grant DE-EE008763 and grant EE0007080 through Utah FORGE. C.M. acknowledges support from the European Research Council Advanced Grant 835012 (TECTONIC), the RETURN Extended Partnership, and funding from the European Union NextGenerationEU (National Recovery and Resilience Plan, Mission 4, Component 2, Investment 1.3, D.D. 1243 2/8/2022, PE0000005). D.E. acknowledges support from EGS Collab funding through LBNL and the G. Albert Shoemaker endowment.
Author contributions: Conceptualization: P.Y. and D.E. Methodology: P.Y., A.E., D.E., and C.M. Investigation: P.Y., A.E., J.W., C.M., and D.E. Visualization: P.Y., D.E., and C.M. Resources: P.Y., C.M., and D.E. Data curation: P.Y., C.M., and D.E. Validation: P.Y., C.M., and D.E. Formal analysis: P.Y., C.M., and D.E. Supervision: C.M. and D.E. Funding acquisition: C.M. and D.E. Project administration: C.M., and D.E. Software: C.M. Writing—original draft: P.Y., C.M., and D.E. Writing—review and editing: P.Y., A.E., J.W., C.M., and D.E. **Competing interests:** The authors declare that they have no competing interests. **Data and materials availability:** All data and code needed to evaluate and reproduce the results in the paper are present in the paper and/or the Supplementary Materials. The dataset used in this study is available at Zendo (https://doi.org/10.5281/zenodo.16891610).

Submitted 24 April 2025
Accepted 5 December 2025
Published 9 January 2026
10.1126/sciadv.ady5201

Science Advances

Seismicity diagnostic of permeability creation from centimeter to subkilometer scales in crystalline rock during shear stimulation

Pengliang Yu, Agathe Eijsink, Junpeng Wang, Chris Marone, and Derek Elsworth

Sci. Adv. **12** (2), eady5201. DOI: 10.1126/sciadv.ady5201

Science Advances (ISSN 2375-2548) is published by the American Association for the Advancement of Science. 1200 New York Avenue NW, Washington, DC 20005. The title *Science Advances* is a registered trademark of AAAS.